Study of disorder in pulsed laser deposited double perovskite oxides by first-principle structure prediction

Edoardo Fertitta[a),1], Sujit Das,[2] Debalina Banerjee,[3] Farbod Ebrahimi,[1] Clément Barraud,[1,4] Kai Du,[5] He Tian,[5] Chris J. Pickard,[6,7] Cedric Weber,[1,3] Ramamoorthy Ramesh,[2] Peter Littlewood,[8] and David Dubbink[1]

[1)] *Happy Electron Ltd, London W3 7XS, United Kingdom*

[2)] *Department of Materials Science and Engineering, University of California, Berkeley, California 94720, USA*

[3)] *Department of Physics, King's College London, London WC2R 2LS, United Kingdom*

[4)] *Laboratoire Matériaux et Phénomènes Quantiques, UMR 7162, Université de Paris, CNRS, 75013 Paris, France*

[5)] *Center of Electron Microscopy, School of Materials Science and Engineering, Zhejiang University, Hangzhou, 310027, China*

[6)] *Department of Materials Science and Metallurgy, Cambridge CB3 0FS, United Kingdom*

[7)] *Advanced Institute for Materials Research, Tohoku University, Sendai, 980-8577, Japan*

[8)] *James Franck Institute and Department of Physics, University of Chicago, Chicago IL 60637, USA*

Double perovskite oxides, with generalised formula $A_2BB'O_6$, attract wide interest due to their multiferroic and charge transfer properties. They offer a wide range of potential applications such as spintronics and electrically tunable devices. However, great practical limitations are encountered, since a spontaneous order of the B-site cations is notoriously hard to achieve. In this joint experimental-theoretical work, we focused on characterisation of double perovskites La_2TiFeO_6 and La_2VCuO_6 films grown by pulsed laser deposition and interpretation of the observed B-site disorder and partial charge transfer between the B-site ions. A random structure sampling method was used to show that several phases compete due to their corresponding configurational entropy. In order to capture a representative picture of most relevant competing microstates in realistic experimental conditions, this search included the potential formation of non-stoichiometric phases as well, which could also be directly related to the observed partial charge transfer. We optimised the information encapsuled in the potential energy landscape, captured via structure sampling, by evaluating both enthalpic and entropic terms. These terms were employed as a metric for the competition of different phases. This approach, applied herein specifically to La_2TiFeO_6, highlights the presence of highly entropic phases above the ground state which can explain the disorder observed frequently in the broader class of double perovskite oxides.

[a)] Corresponding author: edoardo.fertitta@he.co

INTRODUCTION

Double perosvkite oxides $A_2BB'O_6$, in which the B-sites of the unit cell are occupied by different transition metal cations, exhibit a wide range of magnetic and transport properties, ranging from ionic conductivity[1], superconductivity[2], to ferromagnetism[3,4], ferroelectricity[5,6] and multiferroic behavior[7]. Tuning these properties by changes in structure and nature of the A- and B-site cations suggests a variety of potential applications such as magnetic refrigeration[8], and magneto-optic[9] and photovoltaic devices[10]. The properties of these type of materials can depend heavily on the ordering of the B-site cations. For example, the double perovksite La_2MnNiO_6 is a ferromagnet when Ni and Mn are rocksalt ordered at the perovskite B-site, while randomly distributed Mn an Ni gives rise to antiferromagnetic correlations[11]. This is particularly important from the perspective of synthesis. While many interesting properties have been predicted for B-site ordered double perovksite, only few have been realised experimentally[12,13], mainly limited to double perovskites containing B-site ions with large differences in cation size or valency[14,15]. The aim of this work is to investigate the mechanisms behind the difficulties to realise B-site order in perovskite systems, even if an ordered state is thermodynamically favored at first sight[16].

This work focuses on two double perovksites containing different 3d transion metals at the B-site, namely La_2TiFeO_6 and La_2VCuO_6. These materials have in common charge transfer (CT) processes between the B-site ions[17] that can lead to different transition metal oxidation state pairs, i.e. Fe^{3+}/Ti^{3+} and Fe^{2+}/Ti^{4+}, Cu^{2+}/V^{4+} and Cu^{+}/V^{5+}, and correspondingly to different properties. It is tempting to create the conditions allowing for reversible control of these charge transfer processes. In a recent study[18], we predicted via density functional theory (DFT)+U that the charge transfer between Fe and Ti in $LaTiO_3/LaFeO_3$ heterostructures strained on $SrTiO_3$ and $LaAlO_3(100)$ substrates varies sensibly as a function of internal pressure. Also, in this system the charge-transfer mechanism is associated to a tunable ferroelectric behavior since a net polarization of the LaO plane can be created or destroyed as a function of the nominal charge of the TiO_2 and FeO_2 planes.
La_2VCuO_6 also offers interesting possible applications as it is a potential half metal when V and Cu are respectively in the 4+ and 2+ oxidation state and an insulator when V and Cu are respectively 5+ and 1+[19], offering the opportunity to induce a metal-insulator transition by controlling the charge transfer process. However, to our knowledge neither material has been realised experimentally in their B-site ordered double perovksite form, which could be detrimental to the envisioned properties.

This work is dedicated to realization of B-site ordered double perovskite oxides. Pulsed Laser Deposition (PLD) was used to grow La_2TiFeO_6 and La_2VCuO_6 on $SrTiO_3$ (100) and (111) substrates in order to epitaxially stabilise the perovskite phase and potentially use strain to enhance the B-site order[20]. Although high crystalline quality epitaxial perovskite films were made, our experiments confirmed the difficulty of obtaining B-site ordering, which was absent in all our films. In order to guide the design of a controlled growth, an in-depth interpretation of experimental data by high-fidelity modelling becomes necessary. Therefore, the major part of this work is a detailed computational ab-initio study towards the occurrence of disorder in these double perovskites. During growth of the materials, a plethora of structures may compete, and defects can change the energy landscape significantly. This cannot be addressed by searching the ground state of the materials among a few possible candidates, and requires an in-depth exploration of the energy landscape.

Several computational approaches have been successfully applied to the computational sampling of thermodynamically stable compounds, all involving a search for the low-lying energy minima in a high-dimensional configuration space. Evolutionary algorithms such as the Oganov–Glass[21] and Wang's version of particle swarm optimisation[22] are particularly popular. These are based on the idea that a population of structures is evolved by penalising or favouring certain phases as a function of their energy. A different route is taken by random structure sampling methods popularised by implementations such as USPEX[23,24], CALYPSO[25] and the Ab-Initio Random Structure Search (AIRSS)[26–28], which is employed in this investigation. This approach is based upon the structural optimisation of randomly generated structures within chemically intuitive constraints to reduce the size of the explored phase space. The great advantage of such an implementation is its intrinsically highly parallelisability as individual structure relaxations do not depend on each other. Despite its potential high computational cost, the AIRSS method has been applied successfully, for example leading to the discovery of new high pressure phases such as solid hydrogen[29] and ionic ammonia[30].

Random structure sampling offers the advantage of generating more scientific information than characterisation of low-lying states only. In fact, this procedure allows for the mapping of the entire energy landscape, given that the applied constrains allow for it. Therefore, AIRSS lends itself to the handling of configurational entropy[31] if significantly large statistics are collected. The configurational entropy is connected to the size of the basin of attraction of the found structure, which in turn is reflected by the frequency of occurrence of relevant structures[32–37]. The entropic term is also reflected by the density of the energy spectrum which can be evaluated via the entropy forming ability (EFA)[38]. This formalism has been utilised in the past to classify high entropy alloys and predict their relative thermodynamic stability. Herein, the formalism is applied to calculate the amount of competing phases in certain energy window over the whole spectrum, in order to compare the entropy of different structure in the same phase space. Although both these metrics do not capture the role of the vibrational entropy which might be important at higher temperatures, they yield reasonable arguments for the classification of different phases based on their enthalpic and entropic terms.

The computational study of both ground state and growth temperature activated states (within a few hundreds meV from ground state) reveals the presence of competing highly entropic phases above the ground state. These are thought to be responsible for a rich polymorphism leading to the B-site disorder observed via experimental characterisation. Also, the inclusion of different stoichiometries in the computational exploration of the phase space allowed us to explore the role of defects formation on the number of competing phases. Finally, analysis of the distribution of magnetic moments over the whole spectrum revealed how the stoichiometry can affect the magnetic order as well.

RESULTS AND DISCUSSION

Films characterisation

As described in the materials and methods section, pulsed laser deposition was used to grow La_2TiFeO_6 and La_2VCuO_6 films on both (001) and (111) oriented $SrTiO_3$ substrates. The crystalline structure of the films were examined in detail by X-ray diffraction (XRD). As shown in Fig. 1a, the $\theta - 2\theta$ scan of an La_2TiFeO_6 film on a STO (001) substrate indicated presence of a single perovksite phase. The symmetry of the unit cell was investigated by means of reciprocal space mapping.

As shown in Fig. 1e, the La_2TiFeO_6 film was epitaxially strained to the $SrTiO_3$(001) substrate and had a tetragonal symmetry with a=b=3.91 Å, and c=4.01 Å. The high crystalline quality of the film was confirmed by AFM, since a step-and-terrace surface morphology was clearly visible with height differences corresponding to half an unit cell of the double perovskite (Fig. 1c). Similar results were obtained for La_2VCuO_6 films on STO (001) substrates, as shown in more detail in Supplementary Figure 1. The lattice parameters of the La_2VCuO_6 tetragonal cell were a=b=3.91 Å and c=3.97 Å.

Although the films where clearly perovskites, absence of higher order peaks in the XRD $\theta - 2\theta$ scans suggested a random distribution of Ti and Fe (and Cu and V) on the B-site of the perovskite unit cell. The higher order peaks were absent on both (001) and (111) oriented substrates, in both in- and out-of-plane scans, confirming neither planar nor rock-salt ordering of the B-site cations occurred in any of the films. The absence of higher order peaks in out-of-plane scans of thin films on the (001) oriented substrates confirmed the absence of planar ordering (seeFig. 1a). The potential rocksalt ordering on (001) oriented substrates was addressed by performing scans in the [111] direction. Additionally, films were grown on (111) oriented substrates, where any rocksalt would be observable in out-of-plane scans. In both cases, absence of higher order peaks excluded presence of any rocksalt ordering (see Supplementary Figure 1 and 2). The high structural quality and absence of B-site order where confirmed by Scanning Transmission Electron Microscopy (STEM), as shown in Fig. 1d.

Finally, the oxidation states of Fe and Ti where examined by means of X-ray Photoelectron Spectroscopy (XPS). The spectrum of the (001) oriented La_2TiFeO_6 film shown in Fig. 1b reveals that the Fe ions are partly in the 2+ oxidation state, while Ti is completely 4+ (data not shown). The deviation from the expected Fe^{3+} in $LaFeO_3$ and Ti^{3+} in $LaTiO_3$ confirms the occurrence of charge transfer from Ti to Fe when combining these materials in a (B-site disordered) double perovskite. The XPS spectra are comparable to previously published work on $LaTiO_3$/$LaFeO_3$ heterostructures[39]. In both cases, charge transfer leads to partial reduction of the Fe, while a higher degree of reduction is expected based on the complete oxidation of Ti and the predicted electronic structure by DFT[18,39]. In the La_2TiFeO_6 films grown in this work, complete oxidation of Ti could lead to a complete reduction of Fe due the 1:1 ratio of Fe:Ti. The fact that Ti is completely 4+, while only part of the Fe is 2+, highlights that other phenomena beyond the Ti to Fe charge transfer must be responsible for the oxidation of titanium ions. Possible explanations might involve overoxidation during or post growth and La-vacancies.

Both B-site disorder and partial charge transfer may prevent any application of these charge transfer processes. Note that an exhaustive growth study was not performed in this work, and investigation of a much wider growth parameter space needs to be addressed to make firm conclusions about the question whether or not it would be possible to obtain the ordered double perovskites. However, the experimental results are exemplary for a wide range of published results of attempts to grow B-site ordered double perovskites[13].

Simulation of ordered phases

In order to investigate the possible causes of the observed B-site disorder we employed DFT to study the competition of different phases. In this section we will focus on the theoretical investigation of some representative B-site ordered phases. As detailed in the materials and methods section, DFT+U was used to model the strained La_2TiFeO_6 and La_2VCuO_6 films in rock salt and layered phases. Different initial magnetic configurations where chosen in order to stabilise the different (non) CT phases, as detailed more in previous work[18].

As previously reported[18], the ground state of La_2TiFeO_6 is characterised by Fe^{2+} high spin and Ti^{4+} oxidation states. This is a CT state as formal oxidation states in the $LaFeO_3$ and $LaTiO_3$ building blocks are Fe^{3+} and Ti^{3+}, respectively. Minima corresponding to both the CT and non-CT state could be identified by DFT+U for different levels of strain, presenting the same $a^-b^-c^+$ octahedral rotations as the $LaFeO_3$ and $LaTiO_3$ building blocks. Differently, in the La_2VCuO_6 case, the nominal Cu^{3+} and V^{3+} states of bulk $LaCuO_3$ and $LaVO_3$ could not be stabilised in any of the searched minima. Instead, two V→Cu charge transfer states were found. After screening different magnetic orders (see Supplementary Figure 3), we identified the ground state as G-type Cu^{2+}/V^{4+} both for rock-salt and layered orders with the same $a^-b^-c^+$ octahedral rotations as $LaVO_3$. An additional one-electron transfer leads to a non-magnetic state with formal V-d^0 and Cu-d^{10}. These competing states had been previously investigated by means of DFT+U[19], predicting the Cu^{2+}/V^{4+} state to be a half metal for certain choices of U. However, in our case a sensible gap is opened since octahedral rotations are taken into account, while the gap is only reduced when octahedral rotations are suppressed (data not shown).

In order to explore the effect of substrate strains on the relative stability of these different phases and states and hence to predict how these affect the one-electron CT $B \rightarrow B'$ energy gap, we modelled different epitaxial strained phases as described in the materials and methods section. In Fig. 2 we report the energy per formula unit of all La_2TiFeO_6 and La_2VCuO_6 fully relaxed cells calculated for bulk phases and for epitaxially strained phases to model the growth on $SrTiO_3$ and $LaAlO_3$ substrates. In the La_2TiFeO_6 case, the CT state in the rock-salt order is always the most stable configuration, irrespective of the applied strain, and the layered CT state is 200-300 meV above it. Differently, the La_2VCuO_6 G-type ground state shows competition between the rock-salt and layered order within 10 meV per atom and this separation is only slightly enhanced by strain on $LaAlO_3$(100) substrate. This is reflected by the fact that there is a smaller change in the size of the octahedra between the two structures for La_2VCuO_6 than for La_2TiFeO_6 (see Supplementary Table 1). The gap between the Cu^{2+}/V^{4+} and Cu^{+}/V^{5+} exhibit a quite clear phase and strain dependence. Indeed, in the case of rock-salt order it doubles from 200 meV to 400 meV as a function of strain, while it ranges around 800 meV for all structures in the case of a layered order. This can be explained considering the differences in the ionic radii. Cu^{+} is about 25 pm larger than V^{5+}, giving rise to increased strain on the Cu and V octahedra in case of the layered structure[16] (see Supplementary Table 1). On the other hand, the difference between Cu and V ions is reduced for Cu^{2+} and V^{4+} making the layered and rock-salt phases more competitive. In La_2TiFeO_6 the situation is similar for the layered phase, where a large charge transfer gap of 600 meV is observed. However, the CT rock-salt phase is sensibly more stable than the layered one. This cannot be understood in terms of ionic radii alone as Fe and Ti are quite comparable in size.

The predicted competition between rock-salt and layered orders in La_2VCuO_6 justifies the experimentally observed absence of B-site order. Note that controlled formation of Cu^{+}/V^{5+} could favor growth of the rocksalt ordered structure, in agreement with the phase diagram proposed by Ohtomo *et al*[15].

The observed disorder is harder to explain for La_2TiFeO_6 on the basis of these results, as the predicted CT phases do not show any competition. Moreover, the presence of majority of Fe^{3+} in the grown films cannot be understood from the reported calculations alone, since the Fe^{2+}/Ti^{4+} phases are considerably more stable compared to the Fe^{3+}/Ti^{3+} phases. It becomes necessary to investigate more phases which might contribute to the disordered growth. Also, defects such as lanthanum vacancies and the presence of extra oxygen must be included in structure search as they might be responsible of the observed Fe^{2+}:Fe^{3+} ratio.

Random structure search and entropy forming ability analysis

In order to perform this search, the ab-initio random structure search (AIRSS) method was employed. Exploring the vast phase space by means of such a random sampling approach gives us the chance to reveal phases that might be missed by structural optimisation of cells constructed based on chemical intuition. Sampling statistically significant structures via a fast exploration of a vast fraction of phase space will allow to extract thermodynamical meaningful information to understand the nature of the grown films. Although, this will not allow for a description of kinetics of the PLD growth process, characterising the thermodynamically competing phases will lead to describe the driving force dominating during cooling which leads to B-site (dis)order[20]. Indeed, during PLD growth, the high-energy adatoms have diffusion lengths of tens of nanometres which are sufficient to make them migrate and stick to thermodynamically favourable positions. Hence, the grown film will be constituted by a mixture of competing phases contributing to a rich polymorphism or disorder depending on the domain sizes. Since a quantitative calculation of the phase domain sizes goes beyond the scope of this study, in the remainder of the paper we simply will refer to disorder. Also, the information captured by sampling the phase space allows one to explore the role of configurational entropy as well, which yields an additional argument to understand the competition of different microstates which compose disordered structures. Herein, we employ two approaches to qualitatively capture this information, i.e. the relative frequency of occurrence of different phases and the entropy forming ability (EFA).

The first argument is intrinsically connected to the random nature of the structure sampling approach, which in this respect offers a more thermodynamical representation than structure learning based methods. Indeed, frequencies of occurrence of phases obtained by a random sampling search can be related to the volume of the basins of attraction of such minima[32–37], which expresses how accessible these phases are and gives an indication of the configurational entropy. In Fig. 3, the relative frequency of occurrence of the phases within 400 meV of the ground state are shown together with their structures, as predicted by the AIRSS method. In this energy window, five minima were identified, all corresponding to B-site ordered perovskite structures. The rock-salt and layered phases with octahedral rotations $a^-b^-c^+$ described in the previous section were found, and the ground state was predicted to be the rock-salt ordered structure in correspondence to our original structural optimisation. Additionally, a columnar ordered phase was found 50 meV above the rock-salt phase, followed by other distorted rock-salt phases with different octahedral rotations ($a^-b^-c^-$). These findings already add substantial information to the partial picture we depicted in Fig. 2, as the competing phases naturally contribute to the observed B-site disorder.

In addition to the observation of additional phases, a more complex picture emerges from their frequency of occurrence, since the minima above the rock-salt ground state are associated to larger basins of attraction. Similar to the increased occurrence during a random structure search, the larger volume of this basins can be connected to a higher probability of creating these microstates during the PLD growth process. It must be underlined that the amount of sampled structures are not enough to yield a quantitative statistical prediction. However, this contained computational effort is sufficient to sketch a qualitative picture, as the frequencies of occurrence are due to converge with the number of structures.

The data generated by the random structure search can be further analysed by investigating the concentration of minima found in certain energy windows. This constitutes a different way of quantifying configurational entropy and can be described by means of the entropy forming ability (EFA) formalism[38]. This formalism was introduced to capture the predisposition of a material to form high-entropy single-phase crystals by quantifying the number of accessible quasi-degenerate configurations. A high EFA value corresponds to a narrow spectrum which implies the possibility of inducing large randomness (i.e. entropy) at finite temperature. On the other hand, a wide spectrum (low EFA) is associated with the presence of high energy barriers and hence of ordered phases. The EFA can be expressed with the following formula:

$$\mathrm{EFA} = \{\sigma[\mathrm{spectrum}(H_i)]_{T=0\mathrm{K}}\}^{-1} \tag{1}$$

$$\sigma(H_\mathrm{x}) = \sqrt{\frac{\sum_i g_i (H_i - H_x)^2}{\sum_i g_i - 1}} \tag{2}$$

where H_i and g_i are the enthalpy and degeneracy of the collected data points.

In this work this formalism will be utilised in a different way compared to previous works, where an EFA value characteristic of the material is considered. Instead, we calculate the EFA as a continuous function over the whole spectrum to gain insight in how the entropy changes in different energy windows. In this context, the EFA becomes a measure of the expected disorder in the synthetised material. By studying how this is affected by different conditions, one can infer a pathway to optimise the material order. So far we have focused on exploring La_2TiFeO_6 stoichiometric phases only. However, in order to consider more microstates that might emerge in realistic growth conditions, stoichiometric defects cannot be excluded. This is particularly true for overoxidation which might occur not only during growth in oxygen-rich conditions, but also post growth, especially at high temperatures during cool down of the sample. Therefore, we also ran structure searches for unit cells with 25 % La vacancies ($La_{1.5}TiFeO_6$) and for unit cells with 8 % extra oxygen ($La_2TiFeO_{6.5}$). In order to make a fair comparison among the different stoichiometries, the defect formation energies ΔH_f must be considered. If the defects are considered to be charge neutral, the defect formation energy can be expressed as:

$$\Delta H_\mathrm{f} = H_\mathrm{def} - H_0 + \sum n_x (H_x - \mu_x) \tag{3}$$

where H_def, H_0 and H_x are the energy of the relaxed supercell containing n_x defects, the ground state of the perfect system and the elemental reference energy, respectively. The chemical potential of the defect μ_La and μ_O depends on experimental conditions, i.e. partial pressure and temperature. In this work, we considered values ranging between two extremes for the chemical potentials of lanthanum and oxygens which refer to La-poor (μ_La = -8.89 eV), La-rich (μ_La = -3.09 eV), O-poor (μ_O = -3.87 eV) and O-rich (μ_O = 0.00 eV) conditions, following the work of Taylor et al.[40,41]. Since the chemical potential has a large effect on the spectrum, in turn it also affects the EFA as shown in Fig. 4a. The center panel shows the dependence of the EFA in the double-perovskite stability region on μ_O and μ_{La}, reflecting their role on the ability of inducing B-site disorder. As one can see, the disorder is expected to increase in O-rich and La-poor conditions, as the formation of the considered defects becomes more favourable.

It should be underlined that both the frequency of occurrence and the EFA do not fully capture the vibrational entropy which is crucial to describe high temperatures phenomena. However, when comparing similar competing phases to describe the emergence of disorder, the role of the configurational entropy can safely be assumed to be dominating. In the case of La2TiFeO6, the phonon dispersion is dominated by the modes associated to Lanthanum vibrations (see Supplementary Figure 5) which is reasonably very comparable across the competing low-energy phases exhibiting similar volumes and lattice parameters. This yields very similar vibrational contribution for all phases as shown in Supplementary Figure 6 for the rock-salt and layered structure, making the configurational entropy play a major role to drive disorder.

The evolution of the EFA over the energy spectrum is also explored in four corner panels of Fig. 4a for four different conditions. In all cases, the EFA exhibits a maximum ranging between 1.0-2.5 eV depending on the value of μ_{La} and μ_O. The position of this maximum corresponds to the energy window with the highest configurational entropy, i.e. highest density of found minima. As one can see, the effect of μ_{La} on the overall EFA is more impactful than μ_O. This is because $La_{1.5}TiFeO_6$ phases are far more spread over the spectrum than $La_2TiFeO_{6.5}$ phases. For practical applications it is important to focus on the states more easily accessible from the lowest lying phase. In Fig. 4 we highlight the energy window where the ordered perovskites phases reported in Fig. 3 occur, i.e. below 400 meV. It is interesting to note that in this region the EFA increases monotonically as a function of the enthalpy and that such increase depends on the chemical potential being steeper in La-poor and O-rich conditions. This means that several microstates are condensed in this energy window and hence the entropy is larger, possibly causing higher degree of disorder in crystals grown under these conditions.

Finally, we explored the structural and magnetic properties of the phases found during the AIRSS search. In Fig. 4b we report the volume distribution of all minima found by AIRSS in a La-poor and O-poor condition. In the ordered perovskite energy window below 400 meV (in green), all phases (see Fig. 3) have comparable volumes around 130 Å^3 which is in excellent agreement with volumes measured for the films grown on $SrTiO_3$(100) (125 Å^3). For the disordered phases above this energy window a much broader distribution is observed centered around 150 Å^3. Concerning different stoichiometries, the presence of extra oxygens causes a volume expansion and quite a broad distribution with no minima with volumes below 140 Å^3. On the other hand, if La vacancies are included several possible structures with comparable volumes (and compressed) to the ordered perovskites can be obtained.

In order to connect the XPS data presented above to the ab-initio results, we explored the distribution of magnetic moments of Fe and Ti ions across the whole spectrum. These are reported in Fig. 5 where the dominance of different oxidations states are highlighted, based on the values of the magnetic moments. As it can be seen, titanium cations are non magnetic and hence in the Ti^{4+} state for virtually all structures, which fully agrees with XPS data. Similarly, in La_2TiFeO_6 iron cations are always in the Fe^{2+} high spin state, but oxidised Fe^{3+} species emerge in the other stoichiometries. The local intermixing of non-stoichiometric structures with the stoichiometric La_2TiFeO_6 phases is therefore probably responsible of the observed Fe^{2+}:Fe^{3+} ratio.

More experimental and computational analysis has to be performed in order to conclude which non-stoichiometric phases dominate. Presence of lanthanum vacancies (up to 25 %) can be a reasonable explanation, based on similarities between the experimental and computed unit cell volumes. However, inclusion of extra oxygen cannot be excluded, since significant amount of oxygen can be locally added to the La_2TiFeO_6 without destroying the global perovskite structure (see example in Supplementary Figure 4). Finally, other non-stoichiometries should be explored too, such as Ti deficient phases or lower defect concentrations based on larger computational cells.

It is worth stressing the fact that this analysis reflects that non-CT states are extremely unlikely to occur for all stoichiometries considered as Ti^{3+} states are never found. As pointed out above, this is connected to a reduced volume of the basins of attraction and highlights that these states are not easily accessible. This is quite remarkable information that can be obtained by random structure sampling methods. Indeed, although we were able to isolate and characterise these states (see Fig. 2) their existence is irrelevant for practical applications if they cannot be accessed easily.

In conclusion, in this work we employed an ab-initio random structure search method to address the entropic contributions to B-site disorder in double perovskite oxides. High quality La_2TiFeO_6 and La_2VCuO_6 thin films were grown by Pulsed Laser Deposition, but B-site ordering could not be observed. In the case of La_2TiFeO_6, charge transfer from Ti to Fe led to the presence of Fe^{2+}. However, only part of the Fe was reduced, while Ti was completely oxidized, which is contradictory to the complete charge transfer predicted by ab-initio calculations. In order to explain the experimentally observed B-site disorder and oxidation state distributions, a random sampling approach was employed including analysis of defects. Combining the analysis of the frequency of occurrence of the sampled phases and the entropy forming ability we discussed how the configurational entropy rapidly increases above the ground state. The AIRSS search revealed a dense spectrum characterised by several ordered perovskite phases within 400 meV above the ground state. Also, exploration of different stoichiometries, $La_{1.5}TiFeO_6$ and $La_2TiFeO_{6.5}$, yielded a wider overview over the nature of the phases contributing to the observed disorder. The statistically significant phase set sampled by AIRSS was used to constructed a thermodynamic model aiming to understand whether the B-site disorder is due to an intrinsic competition of different phases and/or if tuning experimental conditions might affect it. The EFA analysis suggested that controlling the partial pressure of oxygen and lanthanum in the chamber might minimise the presence of chemical defects, which provides a guide for further experimentation. Nevertheless, the competition of low-energy stoichiometric phases appears to be the dominant factor for the B-site disorder which is much harder to control in an experimental set-up. Although this work does not provide definitive theory for describing the growth of double perovskites, the described insights into the competing phases allowed us to understand the driving force for the observed disorder. The AIRSS study showed presence of non-stoichiometric phases can explain the observed large Fe^{3+}:Fe^{2+} ratio, contrary to the expected absence of Fe^{3+} for stoichiometric phases. This work shows the value of high-throughput ab-initio calculations to investigate formation of realistic but imperfect materials.

METHODS

Experimental setup

45 monolayers La_2TiFeO_6 and 30 monolayers La_2VCuO_6 epitaxial films were synthesised on TiO2 terminated single-crystalline $SrTiO_3$(001) and $SrTiO_3$(111) substrates from stoichiometric ceramic targets via pulsed-laser deposition (248 nm KrF laser). The deposition temperatures of La_2TiFeO_6 and La_2VCuO_6 were 730 ^{o}C and 700 ^{o}C respectively, in an oxygen pressure of 2×10^{-6} Torr. For all materials, the laser fluence was 1.0 J/cm^2, while a laser repetition rate of 1 Hz was used. Reflection high-energy electron diffraction (RHEED) was used during the deposition to ensure a layer-by-layer growth mode. After deposition, the films were cooled down to room temperature at the oxygen pressure used during growth. Structural characterisation of the films were carried out using a Panalytical X'Pert Pro X-ray Diffraction (XRD) diffractometer with Cu-K_α radiation (λ=1.5405 Å). The high crystalline quality of the films was confirmed from $\theta - 2\theta$ symmetric XRD scans around the (002) reflections. The lattice parameters and the tetragonal symmetry are calculated from reciprocal space maps (RSMs) around the (103) reflections. Ex-situ XPS measurements were performed on a PHI VersProbe 3 using monochromated Al-K_α radiation. The TEM measurements were performed at a Cs probe-corrected FEI TITAN operating at 200 kV equipped with a Fischione HAADF detector. The cross-sectional samples were prepared using standard mechanical polishing and dimpling techniques with a final polishing in a Gatan PIPS ion mill using a 3 kV argon beam.

Computational details

All DFT calculations were performed within the Quantum Espresso code (version 6.5) employing the PBE functional and the Hubbard-U local correction in the d-shells of the transition metals. The values for the Ti and Fe were chosen in accordance to the vast literature on DFT+U for similar materials, *i.e.* U(Ti) = 3.0 eV, U(Fe) = 4.8 eV. For La_2VCuO_6 our choice of U-values differs from the referred literature values as they were obtained by means of the self-consistent linear response density functional perturbation theory (DFPT) method proposed by Cococcioni et al.[42] as implemented in Quantum Espresso. The U on vanadium was found to be practically indifferent to the 4+/5+ oxidation states, yielding values of 3.5-4.0eV. On the other hand, the U obtained on Cu^{2+} was around 8.0 eV, while it was undefined for Cu^{+}. This is due to a well known issue with the linear response approach when the correction is applied to filled d-shells. However, since both the energy and the DOS of the non-magnetic state is not strongly dependent on the choice of U, we settled to values of 8.0 eV for a fairer comparison. Plane-wave basis set with an energy cut-off of 800 eV and a $4 \times 4 \times 3$ k-mesh were used with ultrasoft pseudopotentials (USPP) to describe the atomic cores with valence configurations La(4f 5s 5p 5d 6s 6p), Ti(3s 3p 4s 3d), Fe(3s 3p 3d 4s 4p), V(3s 3p 4s 3d), Cu(3s 3p 3d 4s 4p) and O(2s 2p). All calculations were converged to energy <0.1 meV and force <1.0 meV Å^{-1}.

In order to model the growth of the films on different substrates we constrained the surface vectors in accordance to the substrate parameters and allowed for the relaxation along the growth direction as well as of internal coordinates. The initial internal coordinates were chosen to represent the bulk *Pnma* spacegroup symmetry of $LaFeO_3$, $LaVO_3$ and $LaTiO_3$ with octahedral rotations $a^-b^-c^+$. In order to study the effect of B-site in these double perovskites we investigated both the layered and rock-salt order in different magnetic orientations. As the magnetic orientations of all the building blocks is G-type, it is reasonable to believe that it will be maintained also in the heterostructures. It has to be pointed out that in the case of La_2VCuO_6 the situation is not as clear, since $LaCuO_3$ has never been observed experimentally and ab-initio studies debate whether or not it is non-magnetic with a formally Cu^{3+} in a d^9-L state[43–45].

The AIRSS package interfaced with Quantum Espresso was used for the random structure sampling. All searches were performed at 0 GPa, targeting an initial volume of about 125 $Å^3 \pm 20\%$. Distance constraints where imposed by loosing of 20% the interatomic distances in an ordered $LaFeO_3$ perovskite. This allowed to explore a vast number of random sensible structures while respecting the relevant chemistry expected in double perovskites. The ab-initio DFT calculations were performed by sampling on a grid of spacing $2\pi \times 0.1$ $Å^{-1}$ and a plane-wave basis set cutoff of 500 eV. The final structures were further relaxed at the higher level of accuracy reported above. The samplings for La_2TiFeO_6 $La_2TiFeO_{6.5}$ and $La_{1.5}TiFeO_6$ were run separately employing cells consisting 2 formula units imposing random space groups with 2 to 4 symmetry elements. The starting magnetic moments of Ti and Fe ions were also randomly generated. Via the AIRSS sampling a total of 400 random structures were obtained.

In order to test for long-range ordering phenomena, we constructed cells of 4 formula units by elongating the stoichiometric ground state 2 formula unit cell along all lattice vectors, in turn and applying random displacements of the atomic positions up to 0.1 Å. In all cases, the structural relaxations lead to the same minima identified for the smaller cell with energy differences below 10^{-7} eV. Although it would be computationally prohibiting to test this for all phases and stoichiometry considered, the absence of new superstructures in the ground state justify the size for the cell considered.

DATA AVAILABILITY

The data that support the findings of this study are available from the corresponding author upon reasonable request.

ACKNOWLEDGMENTS

Part of this work was performed at the Stanford Nano Shared Facilities (SNSF), supported by the National Science Foundation under award ECCS-1542152. CW was supported by grant [EP/R02992X/1] from the UK Engineering and Physical Sciences Research Council (EPSRC). This work was performed using resources provided by the ARCHER UK National Supercomputing Service and the Cambridge Service for Data Driven Discovery (CSD3) operated by the University of Cambridge Research Computing Service (www.csd3.cam.ac.uk), provided by Dell EMC and Intel using Tier-2 funding from the Engineering and Physical Sciences Research Council (capital grant [EP/P020259/1]), and DiRAC funding from the Science and Technology Facilities Council (www.dirac.ac.uk). CW and DB are grateful to Antoine George, Nicola Bonini and Francesco Macheda for insightful discussions. CJP acknowledges the support of a Royal Society Wolfson Research Merit award. EF and DB thank Matteo Coccioni and Iurii Timrov for useful insights.

COMPETING INTERESTS

The authors declare no competing interest.

AUTHOR CONTRIBUTIONS

R.R., C.W., D.D., C.J.P., C.B. and P.L. designed research; E.F., S.D., D.B., F.E., K.D. and H.T. performed research; E.F., D.D., S.D. and F.E. analysed data; S.D. synthesized and prepared samples; and E.F. and D.D. wrote the paper with input from all the authors.

REFERENCES

[1] López, C. A., Pedregosa, J. C., Lamas, D. G. & Alonso, J. A. The strongly defective double perovskite $Sr_{11}Mo_4O_{23}$: Crystal structure in relation to ionic conductivity. *J. Appl. Crystallogr.* **47**, 1395–1401 (2014).

[2] Rubel, M.H.K. *et al.* Superconducting Double Perovskite Bismuth Oxide Prepared by a Low-Temperature Hydrothermal Reaction. *Angew. Chem.* **126**, 3673–3677 (2014).

[3] Chakraborty, T. *et al.* Disordered ferromagnetism in Ho_2NiMnO_6 double perovskite. *J. Phys. Condens. Matter Mater. Phys.* **29**, 025804 (2017).

[4] Hashisaka, M. *et al.* Epitaxial growth of ferromagnetic La_2NiMnO_6 with ordered double-perovskite structure. *Appl. Phys. Lett.* **89**, 032504 (2006).

[5] Fukushima, T., Stroppa, A., Picozzi, S. & Perez-Mato, J. M. Large ferroelectric polarization in the new double perovskite $NaLaMnWO_6$ induced by non-polar instabilities. *Phys. Chem. Chem. Phys.* **13**, 12186–12190 (2011).

[6] Gou, G., Charles, N., Shi, J. & Rondinelli, J. M. A-Site Ordered Double Perovskite $CaMnTi_2O_6$ as a Multifunctional Piezoelectric and Ferroelectric-Photovoltaic Material. *Inorg. Chem.* **56**, 11854–11861 (2017).

[7] Shimakawa, Y., Azuma, M. & Ichikawa, N. Multiferroic compounds with double-perovskite structures. *Materials* **4**, 153–168 (2011).

[8] Gauvin-Ndiaye, C., Tremblay, A.-M. S. & Nourafkan, R. Electronic and magnetic properties of the double perovskites La_2MnRuO_6 and $LaAMnFeO_6$ (a=Ba,Sr,Ca) and their potential for magnetic refrigeration. *Phys. Rev. B* **99**, 125110 (2019).

[9] Saha-Dasgupta, T. Double perovskites with 3d and 4d/5d transition metals: compounds with promises. *Mater. Res. Express.* **7**, 014003 (2020).

[10] Chen, H. & Millis, A. Design of new mott multiferroics via complete charge transfer: promising candidates for bulk photovoltaics. *Sci. Rep.* **7**, 6142 (2017).

[11] Spurgeon, S. R. *et al.* Competing pathways for nucleation of the double perovskite structure in the epitaxial synthesis of La_2MnNiO_6. *Chem. Mater.* **28**, 3814–3822 (2016).

[12] Shabadi, V. *et al.* Origin of superstructures in (double) perovskite thin films. *J. Appl. Phys.* **116**, 114901 (2014).

[13] Vasala, S. & Karppinen, M. $A_2B'B''O_6$ perovskites: A review. *Progr. Solid State Chem.* **43**, 1 – 36 (2015).

[14] King, G. & Woodward, P. M. Cation ordering in perovskites. *J. Mater. Chem.* **20**, 5785–5796 (2010).

[15] Ohtomo, A., Chakraverty, S., Mashiko, H., Oshima, T. & Kawasaki, M. Spontaneous atomic ordering and magnetism in epitaxially stabilized double perovskites. *J. Mater. Res.* **28**, 689–695 (2013).

[16] Chen, H. & Millis, A. Antisite defects at oxide interfaces. *Phys. Rev. B* **93**, 104111 (2016).

[17] Chen, H. & Millis, A. Charge transfer driven emergent phenomena in oxide heterostructures. *J. Phys. Condens. Matter.* **29**, 243001 (2017).

[18] Lupo, C. *et al.* From Slater to Mott physics: epitaxial engineering of electronic correlations in oxide interfaces. Preprint at `https://arxiv.org/abs/2104.13723` (2021).

[19] Pardo, V. & Pickett, W. E. Evaluation of compensated magnetism in La_2VCuO_6: Exploration of charge states. *Phys. Rev. B* **84**, 115134 (2011).

[20] Kleibeuker, J. E. *et al.* Route to achieving perfect b-site ordering in double perovskite thin films. *NPG Asia Mater.* **9**, e406 (2017).

[21] Oganov, A. R. & Glass, C. W. Crystal structure prediction using ab initio evolutionary techniques: Principles and applications. *J. Chem. Phys.* **124** (2006).

[22] Wang, Y., Lv, J., Zhu, L. & Ma, Y. Crystal structure prediction via particle-swarm optimization. *Phys. Rev. B Condens. Matter Mater. Phys.* **82**, 1–8 (2010).

[23] Lyakhov, A. O., Oganov, A. R., Stokes, H. T. & Zhu, Q. New developments in evolutionary structure prediction algorithm USPEX. *Comput. Phys. Comm.* **184**, 1172–1182 (2013).

[24] Oganov, A. R., Lyakhov, A. O. & Valle, M. How evolutionary crystal structure prediction works-and why. *Accounts. Chem. Res.* **44**, 227–237 (2011).

[25] Wang, Y., Lv, J., Zhu, L. & Ma, Y. CALYPSO: A method for crystal structure prediction. *Computer Physics Communications* **183**, 2063–2070 (2012).

[26] Oganov, A. R., Pickard, C. J., Zhu, Q. & Needs, R. J. Structure prediction drives materials discovery. *Nat. Rev. Mater.* **4**, 331–348 (2019).

[27] Harper, A. F. *et al.* Ab initio structure prediction methods for battery materials a review of recent computational efforts to predict the atomic level structure and bonding in materials for rechargeable batteries. *Johnson Matthey Technol. Rev.* **64**, 103–118 (2020).

[28] Pickard, C. J. & Needs, R. J. Ab initio random structure searching. *J. Phys. Condens. Matter.* **23** (2011).

[29] Pickard, C. J. & Needs, R. J. Structure of phase III of solid hydrogen. *Nat. Phys.* **3**, 473–476 (2007).

[30] Pickard, C. J. & Needs, R. J. Highly compressed ammonia forms an ionic crystal. *Nat. Mater.* **7**, 775–779 (2008).

[31] Reinhardt, A., Pickard, C. J. & Cheng, B. Predicting the phase diagram of titanium dioxide with random search and pattern recognition. *Phys. Chem. Chem. Phys.* **22**, 12697–12705 (2020).

[32] Stevanović, V. Sampling Polymorphs of Ionic Solids using Random Superlattices. *Phys. Rev. Lett.* **116**, 1–5 (2016).

[33] Bartel, C. J. *et al.* Physical descriptor for the Gibbs energy of inorganic crystalline solids and temperature-dependent materials chemistry. *Nat. Comm.* **9**, 4168 (2018).

[34] Jones, E. B. & Stevanović, V. Polymorphism in elemental silicon: Probabilistic interpretation of the realizability of metastable structures. *Phys. Rev. B* **96**, 1–8 (2017).

[35] Krivovichev, S. V. Structural complexity and configurational entropy of crystals. *Acta Crystallogr., Sect. B: Struct. Sci., Cryst. Eng. Mater.* **72**, 274–276 (2016).

[36] Manoharan, V. N. Colloidal matter: Packing, geometry, and entropy. *Science* **349**, 1253751 (2015).

[37] Wilson, B. A., Nasrabadi, A. T., Gelb, L. D. & Nielsen, S. O. Computing free energies using nested sampling-based approaches. *Mol. Simulat.* **44**, 1108–1123 (2018).

[38] Sarker, P. *et al.* High-entropy high-hardness metal carbides discovered by entropy descriptors. *Nat. Comm.* **9**, 1–10 (2018).

[39] Kleibeuker, J. E. *et al.* Electronic reconstruction at the isopolar $LaTiO_3$/$LaFeO_3$ interface: An x-ray photoemission and density-functional theory study. *Phys. Rev. Lett.* **113**, 237402 (2014).

[40] Taylor, F. H., Buckeridge, J. & Catlow, C. R. A. Defects and oxide ion migration in the solid oxide fuel cell cathode material LaFeO3. *Chem. Mater.* **28**, 8210–8220 (2016).

[41] Taylor, F. H., Buckeridge, J. & Catlow, C. R. A. Screening Divalent Metals for A- and B-Site Dopants in $LaFeO_3$. *Chem. of Mater.* **29**, 8147–8157 (2017).

[42] Cococcioni, M. & De Gironcoli, S. Linear response approach to the calculation of the effective interaction parameters in the LDA+U method. *Phys. Rev. B Condens. Matter* **71**, 1–16 (2005).

[43] Mizokawa, T. *et al.* Origin of the band gap in the negative charge-transfer-energy compound NaCuO2. *Phys. Rev. Lett.* **67**, 1638–1641 (1991).

[44] Nohara, Y., Yamamoto, S. & Fujiwara, T. Electronic structure of perovskite-type transition metal oxides $LaMO_3$ (M=Ti-Cu) by U+GW approximation. *Phys. Rev. B Condens. Matter Mater. Phys.* **79**, 1–14 (2009).

[45] He, J. & Franchini, C. Screened hybrid functional applied to 3d0$\rightarrow$3d8 transition-metal perovskites $LaMO_3$ (M=Sc-Cu): Influence of the exchange mixing parameter on the structural, electronic, and magnetic properties. *Phys. Rev. B Condens. Matter Mater. Phys.* **86**, 1–33 (2012).

FIGURE LEGENDS

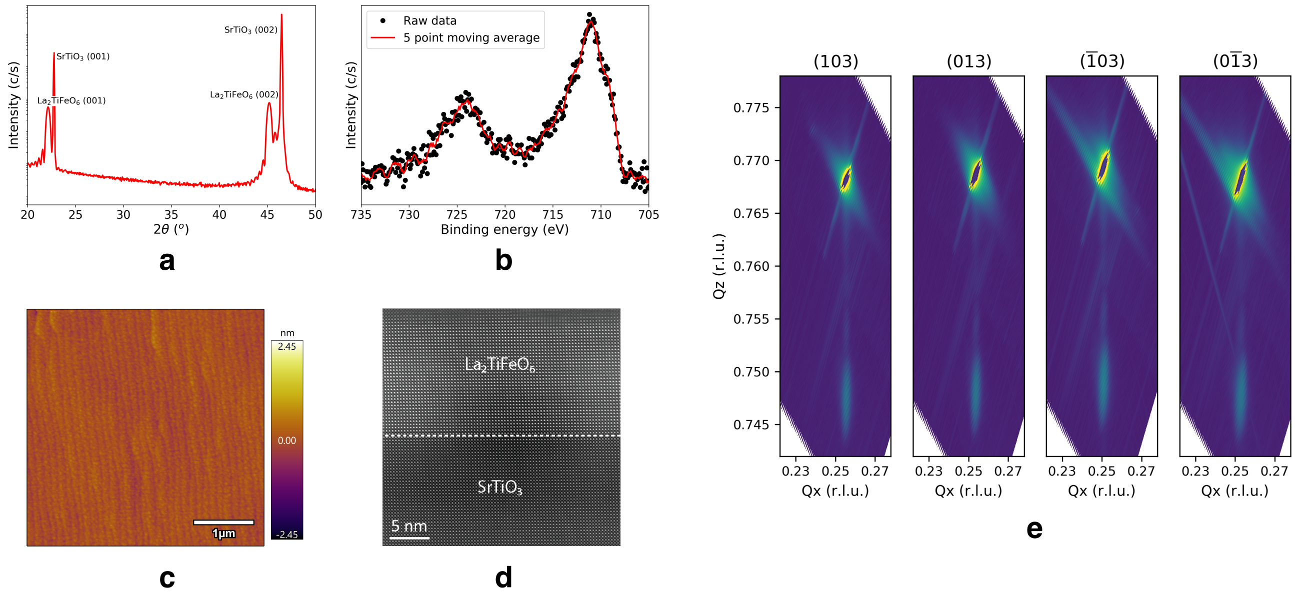

FIG. 1. **Characterisation of a La_2TiFeO_6 film on a $SrTiO_3$ (001) substrate.** XRD **(a)** shows peaks corresponding to single phase perovskite La_2TiFeO_6, but peaks indicating B-site ordering of Ti and Fe are absent. XPS **(b)** shows presence of Fe^{2+} in (001) oriented films, and is visible as a shoulder around 709 eV. XPS additionally shows Ti is completely 4+ (data not included). **(c)** AFM measurements show smooth films with terrace height differences of 0.5 unit cells. Also TEM **(d)** reveals a high structural quality of the grown films and absence of B-site order. **(e)** XRD reciprocal space mapping around the (103) reflection reveals that the strained film exhibit tetragonal symmetry with cell parameters a=3.905 Åand c=4.01 Å.

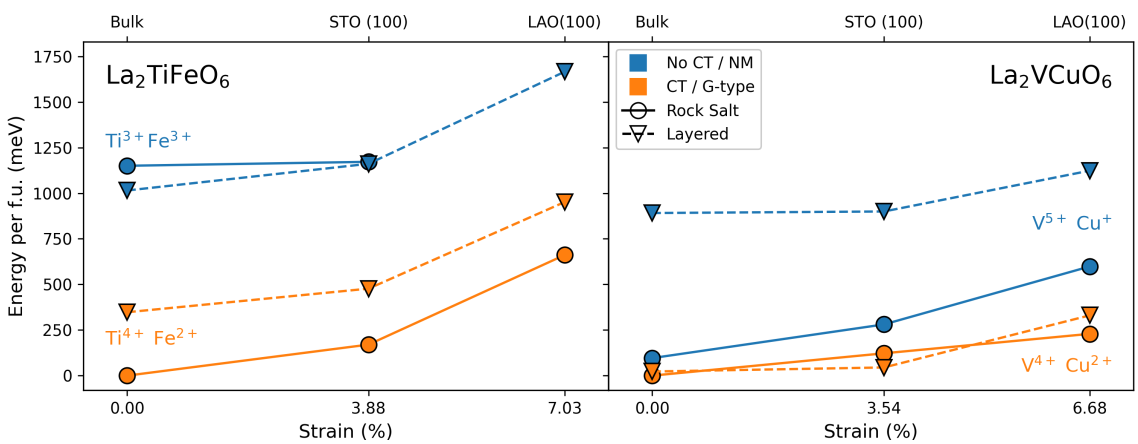

FIG. 2. **Energy differences with respect to the ground state of La_2TiFeO_6 and La_2VCuO_6 ordered phases with different magnetic configurations.** La_2TiFeO_6 and La_2VCuO_6 energy per formula unit of the different states investigated for rock-salt and layered B-site ordering, for bulk phase and for phases strained to $SrTiO_3$ and $LaAlO_3$(100) oriented substrates. Charge transfer and non-charge transfer states are shown for La_2TiFeO_6 while G-type and non magnetic states are shown for La_2VCuO_6.

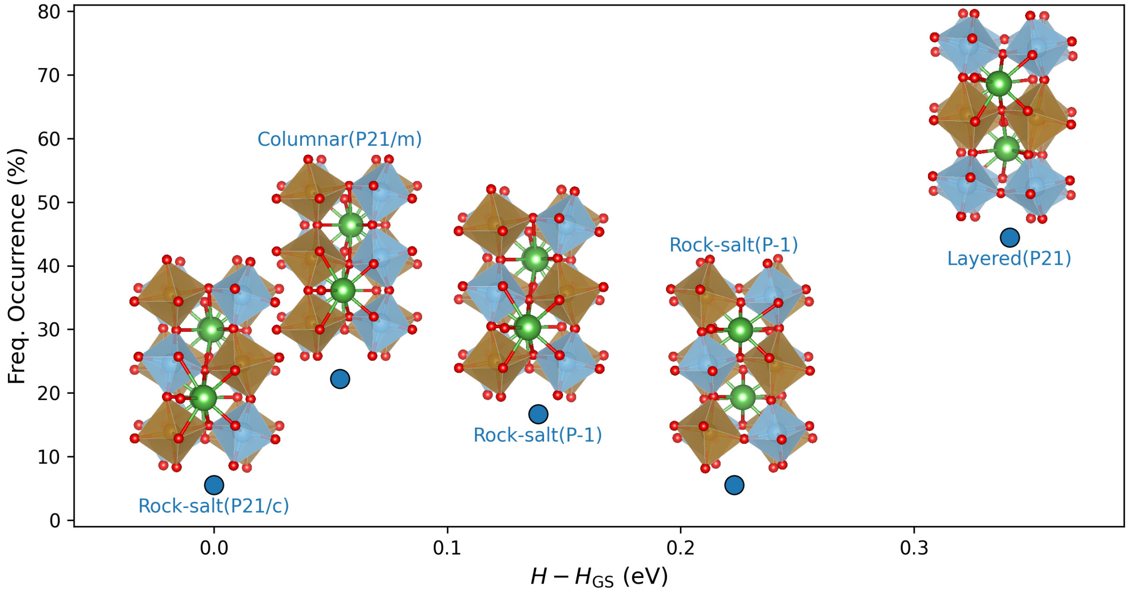

FIG. 3. **Frequency of occurrence of La_2TiFeO_6 perovskite structures captured by AIRSS within 400 meV of the ground state.** The rock-salt with symmetry P_{21}/C was found to occur less often than the columnar and layered phases. Above 100 meV other rock-salt phases with reduced symmetry and different octahedral rotations were found. The competition of these phases and the higher entropy associated with the more frequently occurring phases aligns with the experimentally observed disorder. In the reported structures, the atoms are labelled with different colors: green for La, red for O, blue for Ti and brown for Fe.

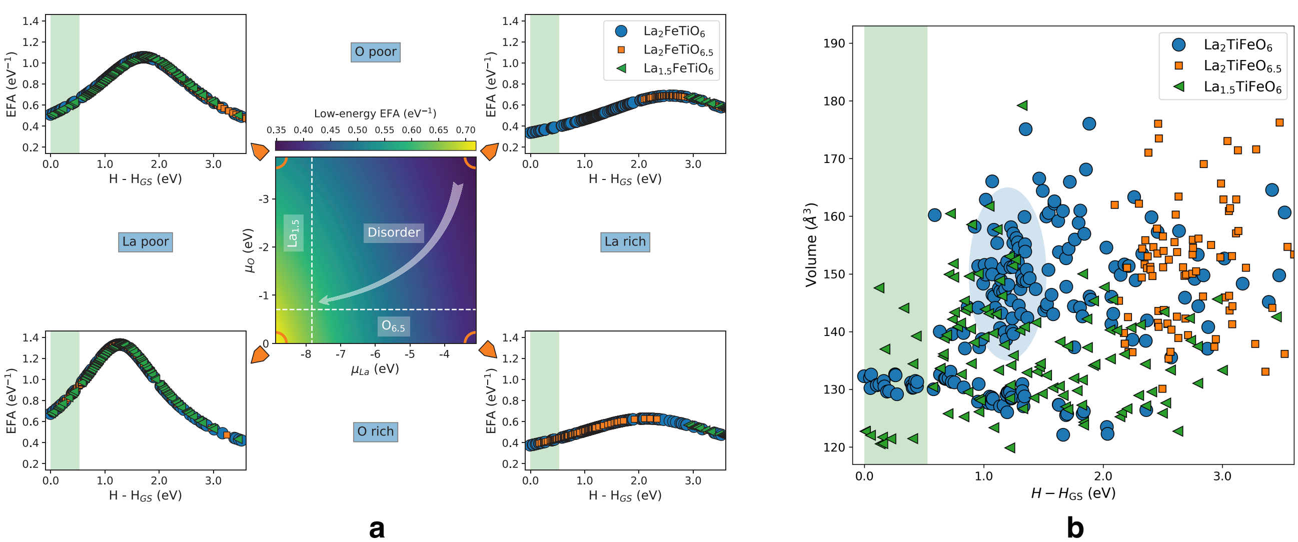

FIG. 4. **EFA analysis of La_2TiFeO_6 (a)** Entropy forming ability analysis of AIRSS results including different stoichiometries in the spectrum. The EFA reflexes the spectrum density and depends on the defect formation energies and hence on the chemical potentials of defects, μ_O and μ_{La}. This is shown in the central panel where we report the EFA calculated in the energy window of stability for double perovskite structures (0-400 meV). This quantity reflects the amount of disorder that can emerge during material growth. The dashed white lines indicate the values of chemical potential, where the considered defects emerge in this energy window and hence contribute to the disorder. The four corner panels show how the EFA changes as La and O poor and rich conditions are considered. The green area highlights the energy window where perovskite structures are observed. **(b)** Volume distribution of AIRSS results including non-stoichiometric phases in La-poor and O-poor conditions. The blue circle highlights encapsules the region with highest state concentration responsible of the maximum of the EFA. All stoichiometric perovskite phases have comparable volumes of about 130 Å^3. Extra oxygen causes a volume expansion, but phases with similar volumes can be obtained by removing 25 % of La.

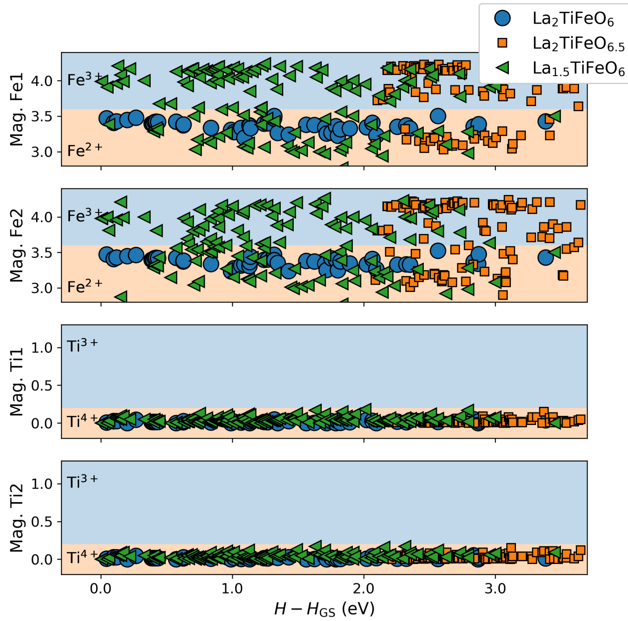

FIG. 5. **Magnetic moments distributions from AIRSS results including the La-poor and O-rich phases**. The distribution for stoichiometric La_2TiFeO_6 is rather homogeneous across the whole spectrum, with the CT Fe^{2+} (HS)/Ti^{4+} CT state as the most likely state. A higher percentage of oxidised Fe^{3+} emerges when defects are included. Ti1, Ti2, Fe1 and Fe2 refer to the different Ti and Fe positions in the unit cell.

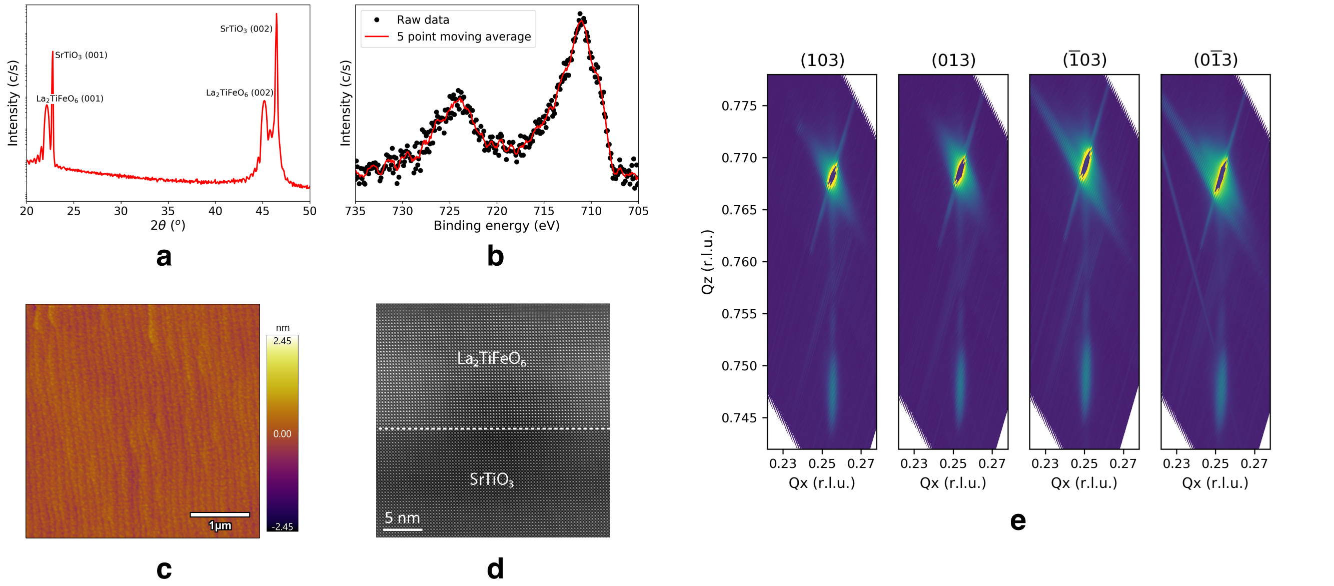
SrTiO3 (002)
SrTiO3 (001)
La2TiFeO6 (001)
La2TiFeO6 (002)
Intensity (c/s)
2θ (°)
a
Raw data
5 point moving average
Intensity (c/s)
Binding energy (eV)
b
nm
2.45
0.00
-2.45
1μm
c
La2TiFeO6
SrTiO3
5 nm
d
(103)
(013)
(1̄03)
(01̄3)
Qz (r.l.u.)
Qx (r.l.u.)
e

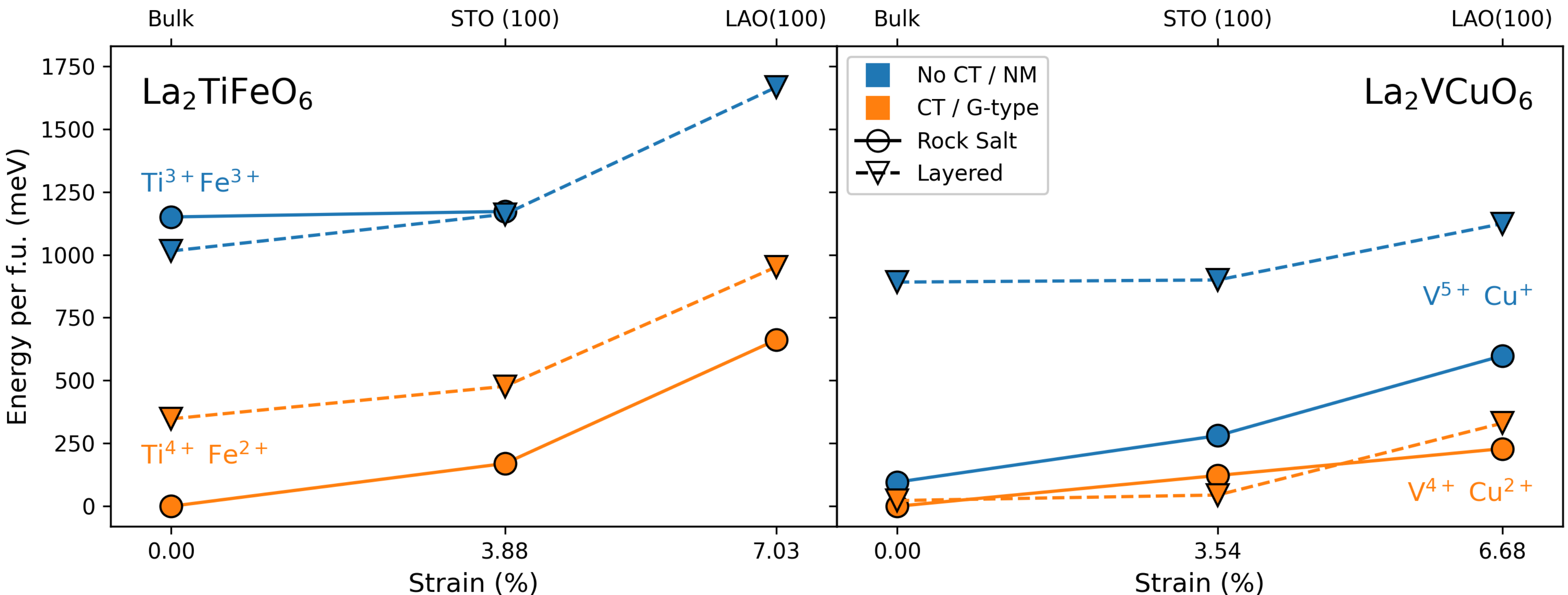

Bulk
STO (100)
LAO(100)
Bulk
STO (100)
LAO(100)
1750
1500
1250
1000
750
500
250
0
Energy per f.u. (meV)
La_2TiFeO_6
$Ti^{3+}Fe^{3+}$
Ti^{4+} Fe^{2+}
No CT / NM
CT / G-type
Rock Salt
Layered
La_2VCuO_6
V^{5+} Cu^{+}
V^{4+} Cu^{2+}
0.00
3.88
7.03
Strain (%)
0.00
3.54
6.68
Strain (%)

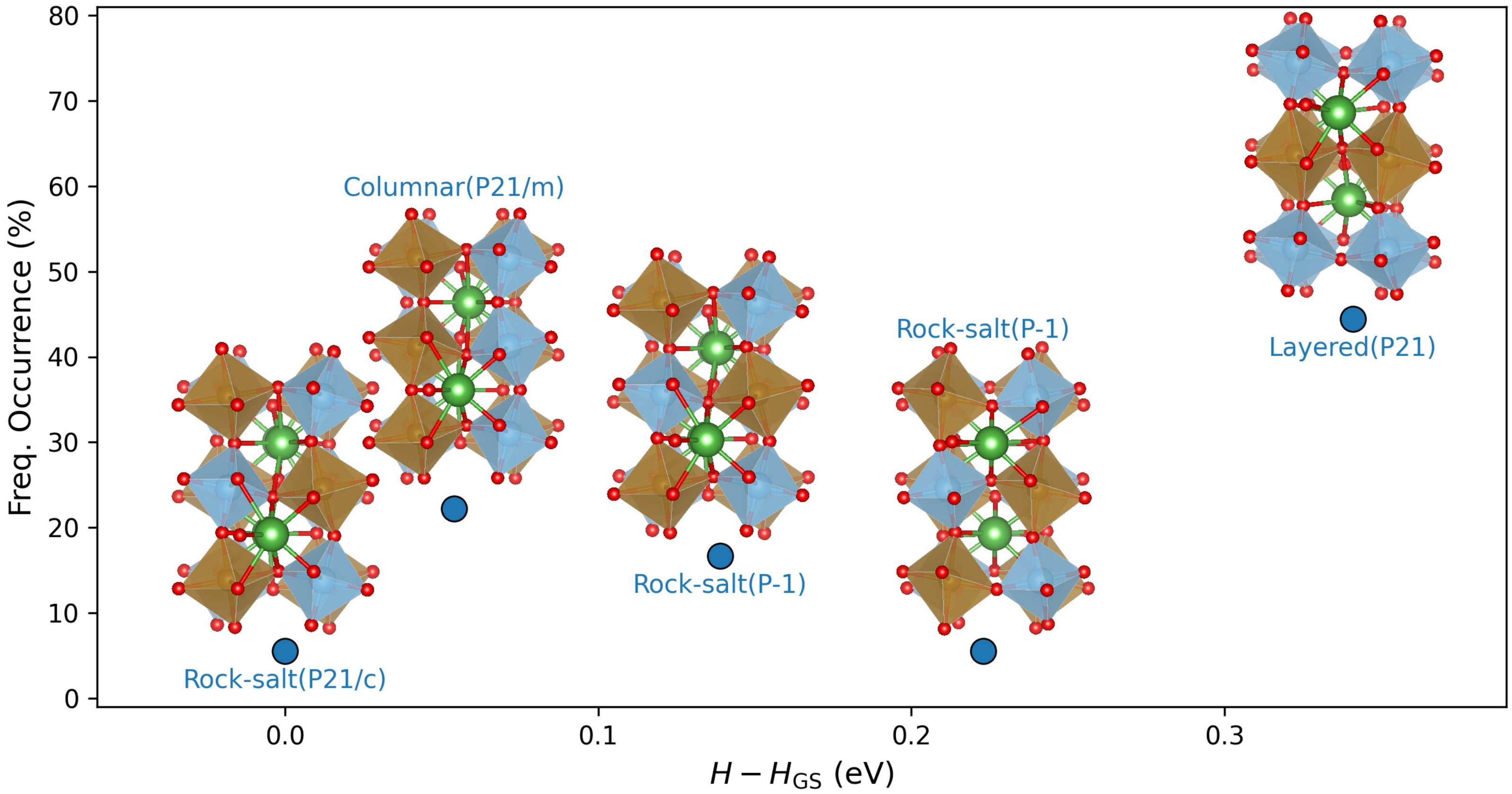

Freq. Occurrence (%)
80
70
60
50
40
30
20
10
0
0.0
0.1
0.2
0.3
$H - H_{\mathrm{GS}}$ (eV)
Columnar(P21/m)
Rock-salt(P-1)
Layered(P21)
Rock-salt(P-1)
Rock-salt(P21/c)


O poor
La poor
La rich
O rich
Low-energy EFA (eV^{-1})
0.35 0.40 0.45 0.50 0.55 0.60 0.65 0.70
Disorder
$La_{1.5}$
$O_{6.5}$
μ_O (eV)
μ_{La} (eV)
EFA (eV^{-1})
H - H_{GS} (eV)
La_2FeTiO_6
$La_2FeTiO_{6.5}$
$La_{1.5}FeTiO_6$
Volume ($\AA^3$)
$H - H_{GS}$ (eV)
La_2TiFeO_6
$La_2TiFeO_{6.5}$
$La_{1.5}TiFeO_6$

a

b

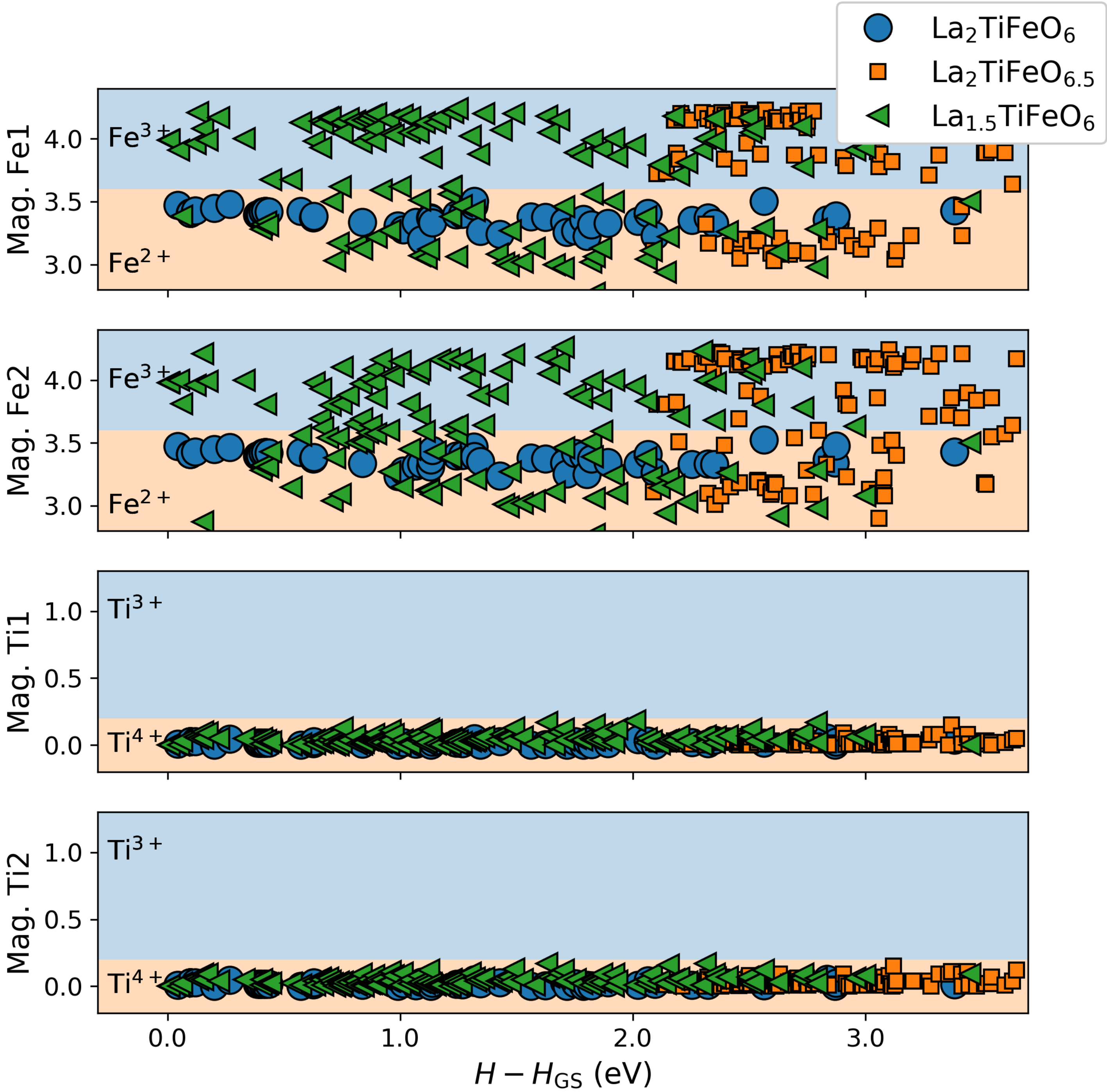

La$_2$TiFeO$_6$
La$_2$TiFeO$_{6.5}$
La$_{1.5}$TiFeO$_6$
Mag. Fe1
Mag. Fe2
Mag. Ti1
Mag. Ti2
Fe^{3+}
Fe^{2+}
Ti^{3+}
Ti^{4+}
$H - H_{\mathrm{GS}}$ (eV)